MATERIALS SCIENCE

A metal-organic framework with ultrahigh glass-forming ability

Ang Qiao,[1] Thomas D. Bennett,[2] Haizheng Tao,[1] Andraž Krajnc,[3] Gregor Mali,[3] Cara M. Doherty,[4] Aaron W. Thornton,[4] John C. Mauro,[1,5,6] G. Neville Greaves,[1,2,7] Yuanzheng Yue[1,5,8]*

Glass-forming ability (GFA) is the ability of a liquid to avoid crystallization during cooling. Metal-organic frameworks (MOFs) are a new class of glass formers (*1*–*3*), with hitherto unknown dynamic and thermodynamic properties. We report the discovery of a new series of tetrahedral glass systems, zeolitic imidazolate framework–62 (ZIF-62) [$Zn(Im_{2-x}bIm_x)$], which have ultrahigh GFA, superior to any other known glass formers. This ultrahigh GFA is evidenced by a high viscosity η (10^5 Pa·s) at the melting temperature T_m, a large crystal-glass network density deficit $(\Delta\rho/\rho_g)_{network}$, no crystallization in supercooled region on laboratory time scales, a low fragility (m = 23), an extremely high Poisson's ratio (ν = 0.45), and the highest T_g/T_m ratio (0.84) ever reported. T_m and T_g both increase with benzimidazolate (bIm) content but retain the same ultrahigh T_g/T_m ratio, owing to high steric hindrance and frustrated network dynamics and also to the unusually low enthalpy and entropy typical of the soft and flexible nature of MOFs. On the basis of these versatile properties, we explain the exceptional GFA of the ZIF-62 system.

INTRODUCTION

Glassy materials are formed in many ways (*4*), among which the most common is to quench a liquid from above the liquidus temperature (T_m) to below its glass transition temperature (T_g) at a rate sufficiently fast to avoid crystallization (*5*). Melt-quenched (MQ) glasses are classified by bonding: covalent, ionic, or metallic. Resistance to crystallization of the melt in the supercooled state can be regarded as a measure of glass-forming ability (GFA), which is commonly inversely associated with the liquid fragility m (corresponding to the activation energy of viscosity η at T_g) (*4*, *5*). GFA is also measured by the ratio T_g/T_m; that is, a liquid with higher T_g/T_m has a higher GFA. Originally empirically defined as the Kauzmann "2/3 Law" (*5*, *6*) and justified for molecular systems (*7*), extending this to other MQ glasses (*1*) reveals considerable variability in T_g/T_m. Systems with $T_g/T_m > 2/3$ have a high GFA because they are increasingly viscous throughout the reduced supercooled state, which inhibits crystallization. In some instances, crystallization is completely absent on laboratory time frames, notably for B_2O_3 glass (*8*), where there is a significant crystalline-glass density difference $\Delta\rho/\rho_g$, but also for acrylic glasses such as poly(methyl methacrylate) (PMMA) (*9*), where crystallization is blocked by the random orientation of side and pendent groups (atacticity).

The structural rules for glass formation are well established (*5*) and, for oxide glasses, result in Zachariasen's continuous random network (CRN) model of corner-sharing cation polyhedra, recently confirmed through transmission electron microscopy images (*10*). Subsequently, a simplified model based on a topological optimization of the noncrystalline network was introduced (*11*), which has been reduced to a purely mathematical condition for the formation of infinitely large, topologically disordered networks of arbitrary dimensionality (*12*) and explored in detail for metallic and oxide systems (*13*).

[1]State Key Laboratory of Silicate Materials for Architectures, Wuhan University of Technology, Wuhan 430070, China. [2]Department of Materials Science and Metallurgy, University of Cambridge, Cambridge CB3 0FS, UK. [3]Department of Inorganic Chemistry and Technology, National Institute of Chemistry, 1001 Ljubljana, Slovenia. [4]Future Industries, Commonwealth Scientific and Industrial Research Organisation, Clayton South, Victoria 3168, Australia. [5]School of Materials Science and Engineering, Qilu University of Technology, Jinan 250353, China. [6]Department of Materials Science and Engineering, The Pennsylvania State University, University Park, PA 16802, USA. [7]Department of Physics, Aberystwyth University, Aberystwyth SY23 3BZ, UK. [8]Department of Chemistry and Bioscience, Aalborg University, DK-9220 Aalborg, Denmark. *Corresponding author. Email: yy@bio.aau.dk

Recently, a new family of MQ glasses has emerged, derived from crystalline metal-organic frameworks (MOFs), where metal nodes are linked by organic ligands through coordination bonds (*1*–*3*). A subset of MOFs, zeolitic imidazolate frameworks (ZIFs), adopts similar structures to zeolites (*14*), where metal ions (for example, Zn^{2+} and Co^{2+}) replace SiO_4 and AlO_4^- tetrahedra, linked by rigid organic ligands (*15*) in place of less-constrained bridging oxygens (Fig. 1A) (*5*). Although more than 60,000 MOF (*16*) or associated coordination polymer (CP) structures (*2*) exist, few reports document their melting behavior because decomposition usually intervenes (*1*). Nevertheless, a growing number of MQ MOF glasses are being presented (*1*–*3*, *17*, *18*). Here, we report the discovery of ultrahigh GFA in the ZIF-62 system.

ZIF-62 is a mixed-linker framework of nominal composition $Zn(Im)_{1.75}(bIm)_{0.25}$ in which Zn^{2+} is coordinated to imidazolate (Im) ($C_3H_3N_2^-$) and benzimidazolate (bIm) ($C_5H_7N_2^-$) ligands whose orientation alternates along the tetrahedral lines (*15*) and whose proportions can be altered (Fig. 1A). With combined linkers, ZIF-62 undergoes only a single melting event before decomposition upon heating, with fusion being uninterrupted by intermediate polyamorphism and crystallization, in contrast to ZIF-4 [$Zn(Im)_2$] (*1*). Overall, the structure of ZIF-62 is analogous to the classical CRN model for silica (Fig. 1A); however, the tetrahedral units are far larger than those of oxide glasses, and the two-body Zn-N and three-body N-Zn-N constraints, if they can be preserved through melting, are much weaker.

Glass formation of some ZIF crystals, including ZIF-62, was reported in a recent paper (*17*), where it was demonstrated that the melting temperature and dynamical parameters (for example, T_g and liquid fragility) of the glass-forming ZIFs could be tuned by changing their chemistry (for example, linker type) and framework topology. Very recently, the melting behavior of ZIF-4 has been explored by performing structural analysis and first-principle molecular dynamics simulations (*19*). In contrast to these studies, we focus on determining and understanding the GFA of both standard and nonstoichiometric ZIF-62 liquids. We demonstrate that supercooled ZIF-62 liquids have an extremely high viscosity ($\eta = 10^{5.1}$ Pa·s) at T_m, show no signs of crystallization at high T/T_m ratios, and have T_g/T_m ratios greater than any other MQ glass (inorganic, organic, or metallic). We clarify the origins of this highly striking glass-forming behavior by varying proportions of Im and bIm framework linkers, using differential scanning calorimetry

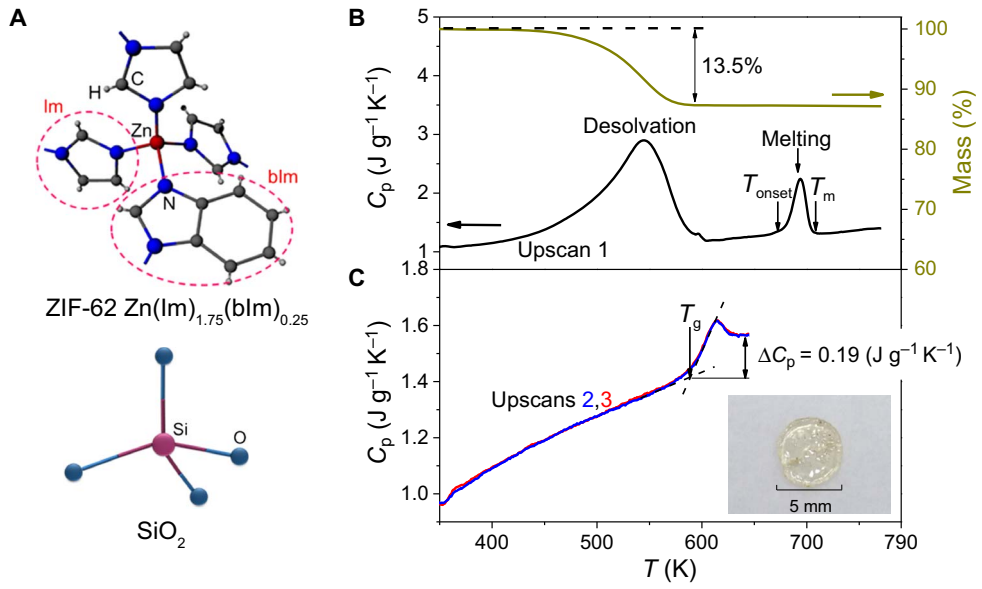

Fig. 1. Structural units and calorimetry of ZIF-62. (**A**) Similarity between tetrahedra in silicate glasses and ZIF-62 Im/bIm networks. (**B**) C_p and mass loss versus T, heated at 10 K min^{-1}, following desolvation to eventual melting at T_m = 708 K. (**C**) C_p upscans of ZIF-62 glass quenched from above T_m showing a clear glass transition (T_g = 595 K), yielding T_g/T_m (0.84). Inset: Optical image of a transparent MQ glass.

(DSC) to quantify T_g, T_m, m, melting enthalpy (ΔH_m), and entropy (ΔS_m); by determining η at T_m; and by using a combination of spectroscopies and diffraction to establish structural connectivity and internal pore geometry. Aside from direct insight into the GFA of a new category of glass systems, the work also contributes to clarifying the general features of the glass transition, which remains the challenging problem in condensed matter physics (*20*).

RESULTS

Figure 1B shows the isobaric heat capacity (C_p) curve obtained during the first DSC upscan, where we can observe the enthalpy response to the solvent release and the melting process (characterized by T_m). Figure 1C exhibits the C_p curves obtained during the second and third DSC upscans, where we can see the glass transition (characterized by T_g). The T_g/T_m is found to be 0.84, which is significantly higher than the empirical "2/3 rule." The MQ ZIF-62 is transparent and fully noncrystalline after soaking for 24 hours close to T_m (Figs. 1C, inset, and 2A and fig. S1). X-ray photoelectron spectroscopy (XPS) bands for Zn, N, and C orbitals of ZIF-62 crystal and MQ glass overlap almost perfectly (fig. S2), implying no obvious electronic structural differences. The total scattering x-ray diffraction (XRD) atomic radial distribution functions $D(r)$ for ZIF-62 and the derived MQ glass share virtually the same infratetrahedral correlations and amplitudes, chiefly from Im, confirming common geometries and rigidity (Fig. 2B). However, the interatomic correlations become weaker and broader in the MQ glass, indicative of tetrahedra and bridging angle disorder analogous to long-range order in CRN oxide glasses, which seldom persists beyond 2 nm (*5*). In addition, the Raman data for ZIF-62 and MQ glass reflect nearly the same frequencies and strength of infratetrahedral vibrations (Fig. 2C), endorsing the integrity of organic linkers being retained in the MQ glass, consistent with the simulation results for ZIF-4 (*19*). However, there are some changes from crystal to glass: (i) The Zn-N stretching mode (*21*) becomes non-Gaussian and increases in frequency, and (ii) the C-N mode (*22*, *23*) decreases in frequency. Both effects indicate small adjustments in the glass tetrahedral dynamics compared to ZIF-62, consistent with network disorder and flexibility.

Regarding $\Delta\rho/\rho_g$, the MQ ZIF-62 glass is slightly denser than its original crystalline state (*17*), as the case of zeolites (*5*, *14*). However, there are considerable differences between the internal pore volume fraction for ZIF-62 (27%) (*17*) and that for the MQ glass (6%), which was revealed by positron annihilation lifetime spectroscopy (PALS) (figs. S3 and S4 and table S2) (*24*). This large difference indicates that the density of the network surrounding the pores in ZIF-62 is far higher than the equivalent CRN network enveloping the fewer pores in the glass, pointing to a far more dilated and disordered topology of the glass than the parent crystal (see the Supplementary Materials).

Another very important contributory factor to the ultrahigh GFA of MQ ZIF-62 glass is its unusually high viscosity η ($10^{5.1}$ Pa·s) at T_m (Fig. 2D), which is a first insight into MOF-liquid viscosities. Interpolated from fitting the MYEGA equation (*25*), this is comparable to that of silica at T_m ($10^{5.5}$ Pa·s) (*25*). The fragility index m of liquid ZIF-62 obtained from DSC is 23 (fig. S5), a small value comparable to that of silica (m = 20) (*26*), confirming the exceptionally strong nature of supercooled ZIF-62 and with the high η(T_m) and explaining, for instance, why sintering powdered samples do not achieve appreciable flow until T_m is exceeded (fig. S6).

To suppress crystallization below T_m, the cooling rate must be significantly faster than the crystal growth kinetics. For strong liquids such as silica and ZIF-62, viscous flow and crystal growth are fully coupled (*26*). Silica has one of the lowest growth rates U_{max} close to T_m over 24 hours, leading to micrometer crystallites being readily detectable optically. The absence of detectable crystallization when ZIF-62 glass is held close to T_m for similar periods (Fig. 2A) indicates even lower U_{max}, commensurate with its superior GFA. This resistance to recrystallization is consistent with the diffusing units in ZIF-62 being much larger than in oxide systems so that their migration is mutually conflicted.

The effects of framework composition on the microstructure and thermodynamic properties of the ZIF-62 systems and MQ glasses were

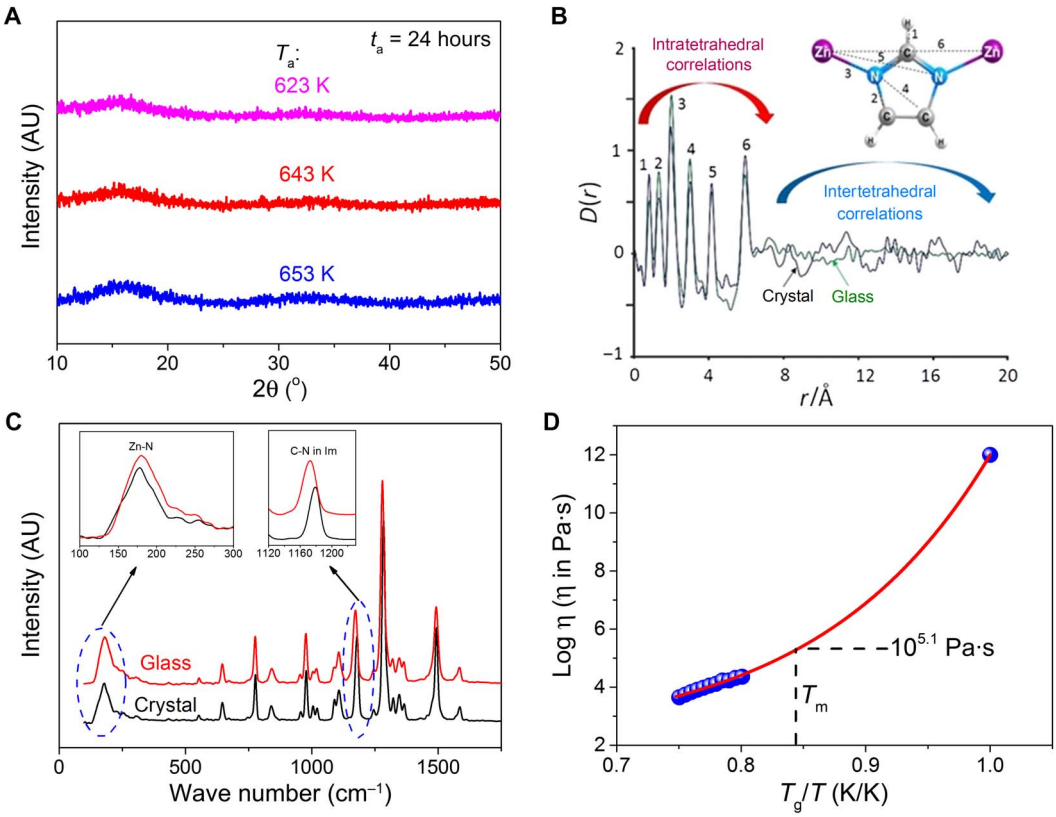

Fig. 2. ZIF-62 ultrahigh GFA, high viscosity at T_m, and crystal-glass structural evolution. (**A**) XRD patterns of ZIF-62 glasses in argon at temperatures approaching T_m (0.88 < T/T_m < 0.92) for t_a = 24 hours. AU, arbitrary units. (**B**) Crystalline and glass pair distribution functions $D(r)$ with Im geometry identifying peaks 1 to 6, which are replotted from the study of Bennett *et al.* (*17*). (**C**) Raman spectra of crystal and glass. Insets: Changes in nodes (Zn-N) and linkers (C-N). (**D**) Temperature dependence of η for bIm/(Im + bIm) = 0.125 liquid with MYEGA (Mauro-Yue-Ellison-Gupta-Allan) fit (*25*). A two-parallel plate oscillation technique was used to avoid high-temperature oxidation, the first η measured for any MOF liquid.

inspected by nuclear magnetic resonance (NMR) spectroscopy. ^{1}H solution NMR spectra of the dissolved samples (fig. S8 and table S3) (*1*, *27*) showed that bIm/(Im + bIm) ratios for crystals and glasses were equal (Fig. 3A), demonstrating that no decomposition or volatilization occurred during melting and that Zn-N and N-Zn-N constraints and linker conformation survived melting. ^{1}H-^{13}C cross-polarization magic-angle spinning (CPMAS) solid-state NMR spectra distinguish the signals that belong to the different C sites of bIm and Im in crystalline ZIF-62 systems and reflect the structural evolution with increasing bIm/(Im + bIm) ratio (Fig. 3B and figs. S10 and S11). More demanding carbon-detected ^{1}H spin-diffusion NMR spectroscopy confirmed that bIm and Im linkers were intimately mixed within nonstoichiometric ZIF-62 frameworks (that is, the framework with compositions deviating from that of standard ZIF-62) and indicated that, with the increasing bIm content, not only tetrahedral nodes with one bIm and three Im linkers but also tetrahedral nodes involving two bIm linkers start to appear (figs. S12 and S13). This is an indirect implication that the substitution of bIm for Im takes place in a random manner, without bIm clustering.

DISCUSSION

The retention of Zn nodes with mixed linkers through melting to vitrification (Fig. 2) contrasts with the breakup of stable tetrahedral arrangements when some CP systems melt (*2*). The additional steric hindrance of mixed linkers in nonstoichiometric ZIF-62 contributes to the extraordinarily high η(T_m) and keeps the similar topology of the hybrid network frozen into the glass. Both T_m and T_g rise with increasing bIm (Fig. 3C and fig. S9); however, T_g/T_m ratios remain constant (0.84), confirming the ultrahigh GFA of MQ ZIF-62 glasses (Figs. 1 and 2). The rising trends of T_m and T_g with increasing bIm indirectly confirm that the added bIm linkers uniformly and randomly substitute the Im linkers in the tetrahedral network, and hence, the Zn-linker tetrahedron becomes larger, leading to stronger steric hindrance.

The entropy and enthalpy of fusion of nonstoichiometric ZIF-62 (ΔS_m and ΔH_m, respectively) also rise linearly with increasing bIm/(Im + bIm) (see table S2). ΔS_m increase illustrates how bIm ligands enhance the number of configurational states at T_m (Fig. 3D). It is also comparable to the configurational entropy S_{config} retained in silica at its glass transition (see the Supplementary Materials) (*28*), reflecting the softer structure of MOFs. Likewise, the increase of ΔH_m demonstrates that the bulkier linker demands more thermal energy to initiate structural reconfiguration at the onset of melting. Nevertheless, ΔH_m is over two decades smaller than that for quartz (see the Supplementary Materials). In addition, the rising of ΔS_m and ΔH_m with bIm/(Im + bIm) also implies that the added bIm linkers chemically participate in the structural network in a random manner.

Finally, GFA in terms of T_g/T_m for ZIF-62 is compared in Fig. 4 with that for 50 other glasses. With T_m's ranging more than 1800 K, traditional glasses fall on either side of 2/3 value for glass formation (*5*, *6*). It

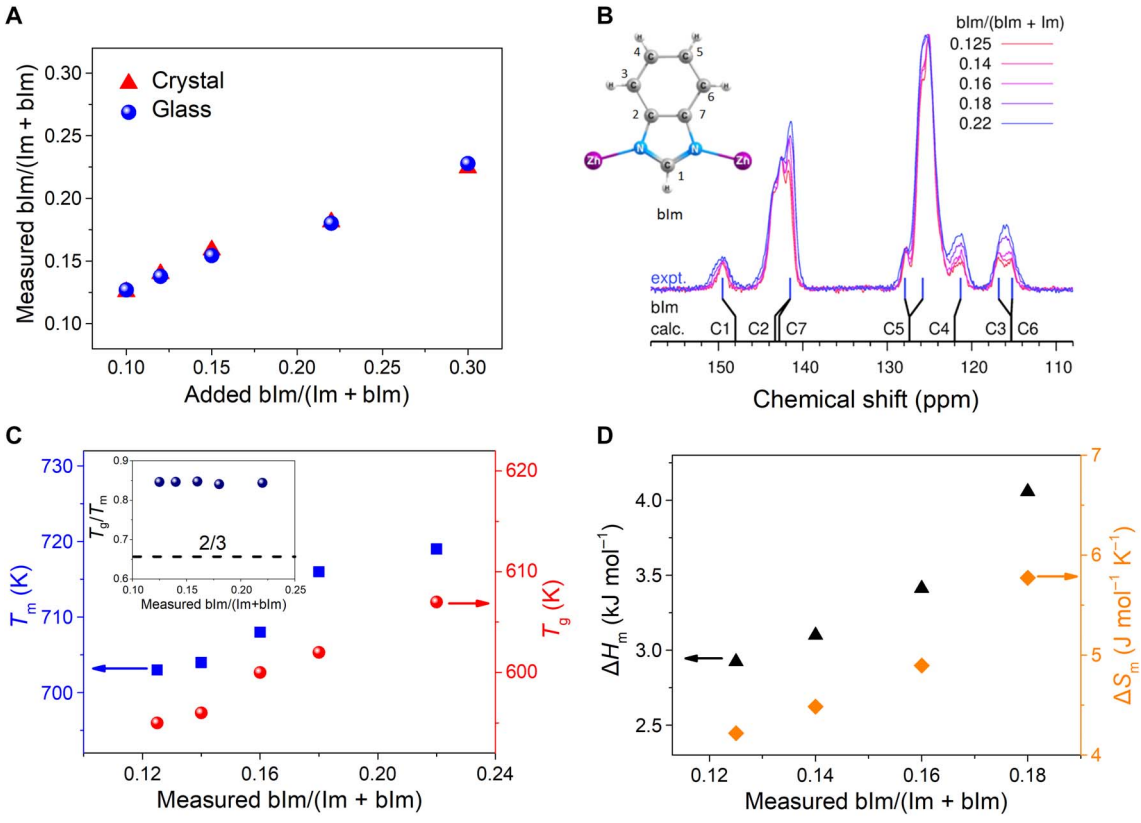

Fig. 3. Effects of linker substitution on microstructure and thermodynamic characteristics. (**A**) blm/(Im + blm) ratios in both ZIF-62 crystal and glass from ^{1}H liquid NMR (see the Supplementary Materials) versus synthesized values. The crystal structure was checked through XRD patterns (fig. S7). (**B**) ^{1}H-^{13}C CPMAS NMR spectra of crystalline samples of ZIF-62 with varying blm/(Im + blm) ratio highlighting blm contributions [calculated shifts in black (see the Supplementary Materials)]. ppm, parts per million; expt., experiment; calc., calculation. (**C**) Increase in T_m and T_g with increasing blm. Inset: Almost constant T_g/T_m for mixed linkers, compared to the 2/3 rule (*5*–*7*). (**D**) Increases in ΔH_m and ΔS_m on fusion with increasing blm.

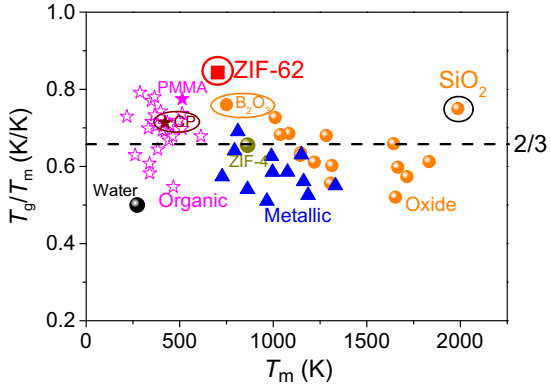

Fig. 4. The ultrahigh T_g/T_m ratio of ZIF-62. The comparison in T_g/T_m ratio between ZIF-62 and other types of glass-forming systems, including water (*29*, *30*), oxide (*33*), metallic (*34*), and organic (*35*, *36*)—good GFA typified by CPs, PMMA, B_2O_3, and SiO_2 in contrast with the ultrahigh GFA of the ZIF-62.

shows that T_g/T_m (0.84) of ZIF-62 is the highest of the 50 glasses, indicating its ultrahigh GFA. T_g/T_m of water is adopted as 0.5 in Fig. 4, and T_g is explained in table S4 (*29*, *30*). In contrast, ZIF-4 has a T_g/T_m of 2/3 and amorphizes before crystallizing to ZIF-zni and subsequent melting but has a similar $\Delta\rho/\rho_g$ value to that of water. Ranked below ZIF-62 but with $T_g/T_m > 2/3$ are the following glass formers: CP with weakly interacting linear chains has transitory GFA, very low $\eta(T_m)$, and reversible crystallization and melting (*2*); SiO_2 glass with high $\eta(T_m)$, but with low $\Delta\rho/\rho_g$, weakly recrystallizes close to T_m (*26*); both PMMA and B_2O_3 glasses show no signs of recrystallization but for different reasons. The structure of PMMA sterically hinders periodic arrangement (*9*), whereas B_2O_3 with its boroxol ring structure is topologically remote from any candidate crystal, leading to a huge $\Delta\rho/\rho_g$ (*8*). These metrics factor into the ultrahigh GFA discovered for ZIF-62 glasses with their uniquely high T_g/T_m and will influence the search for other MQ glasses that resist crystallization on laboratory time scales. Randomly distributed bulky linkers, such as bIm, inhibit recrystallization, as does the large network density deficit $(\Delta\rho/\rho_g)_{network}$, making $\eta(T_m)$ comparable to that of SiO_2 (*28*), traditionally the most viscous and strongest of inorganic liquids.

Because melting of ZIF-62 must involve complementary processes that lead to the enhanced GFA, three aspects of the melting mechanism emerge: (i) The central tetrahedral node acquires Lindemann kinetic energy (~k_bT_m), which weakens Zn-N coordination bonds, breaks crystalline periodicity, shrinks pores, eliminates channels, and generates and randomizes clusters, chains, and rings; (ii) flowing nanosized structural units experience strong steric hindrance, resulting in viscous cooperative translational motion; (iii) the equilibrium between Zn-N bond deconfiguration and reconfiguration and altered conformation of linkers leads to a much expanded network compared to the porous ZIF-62. All of these suggest that a compromise between porosity, flexibility, and

viscosity in MOF liquids may be necessary to facilitate applications involving guest separations in sintered MOF glass bodies.

Furthermore, ZIF-62 glass exhibits an ultrahigh Poisson's ratio (ν = 0.45), which is in strong contrast to that (0.15) of its counterpart, the ZIF-62 crystal. The two ratios are located on the opposite sides of the brittle-to-ductile transition (fig. S14) (*31*), where the fracture energy scales abruptly. Physically, ν distinguishes harmonic response where compression is compromised to retain shape (ν→0) from incompressibility at the expense of shape (ν→0.5). Accordingly, MQ ZIF-62 is far less compressible than ZIF-62. Such a large difference should be a contributing factor inhibiting recrystallization, either from the glass (ν = 0.45) or from the supercooled liquid (ν = 0.5).

MATERIALS AND METHODS

Synthesis

ZIF-62 was synthesized using $Zn(NO_3)_2{\cdot}6H_2O$ (Zn; 99.99%) as the metal source, Im (99.5%) and bIm (99%) as the linkers, and *N*,*N*′-dimethylformamide (DMF; 99.9%) as the solvent. The Zn (0.2 M), Im (1.5 M), and bIm (0.2 M) stock solutions were prepared by dissolving the above mentioned precursors in DMF. The appropriate volumes of the stock solutions were mixed together according to the reagent Zn/Im/bIm molar ratio of 1:13.5:1.5. The solutions were mixed in a 100-ml Teflon-lined autoclave, stirred for 1 hour, and then placed in an oven at 403 K for 96 hours. Subsequently, the Teflon-lined autoclave was cooled to ambient temperature. The solid was washed three times in DMF and dried at 373 K for 4 hours. The crystalline nature of the as-prepared sample was confirmed by the XRD pattern. Moreover, to explore linker compositional effects on melting and glass formation, we changed the ratio between bIm and Im in ZIF-62 during synthesis according to the strategy outlined in table S1. The MQ ZIF-62 glass samples were obtained by heating the crystalline ZIF-62 powder to 773 K in argon in the DSC. The glass samples for mechanical tests were produced by using a melting-pressing approach in a vacuum furnace.

Measurements

Calorimetric analysis

The DSC characterizations of all the samples were conducted using a Netzsch STA 449 F1 instrument. The samples were placed in a platinum crucible situated on a sample holder of the DSC at room temperature. The samples were held for 5 min at an initial temperature of 313 K, heated at 10 K min^{-1} to the target temperature, and then cooled back to 473 K at 10 K min^{-1}, thus forming the standard glass (*32*). After natural cooling to room temperature, the second upscan was performed using the same procedure. To determine the C_p of the samples, both the baseline (blank) and the reference sample (sapphire) were measured.

Powder XRD

Room temperature powder XRD data (2θ = 5° to 40°) were collected with a Rigaku-RU 200B diffractometer using Cu K_α (λ = 1.540598 Å) radiation.

Viscosity

The viscosity of ZIF-62 liquids was measured in the temperature range from 743 to 793 K above T_m in flowing nitrogen atmosphere on a rheometer (TA Discovery HR-2) with a parallel-plate geometry (diameter, 25 mm) at the strain of 0.1%. However, it was not possible to measure the viscosity data around T_g due to lack of a viscometer that could avoid the oxygen influence. On the other hand, it was easy to measure the T_g and the liquid fragility index *m*. We combined the high-temperature viscosity data above T_m and the viscosity value (10^{12} Pa·s) at T_g and then fitted these data to the MYEGA viscosity model (*25*) to get the fragility index *m*. Thus, we were able to extend the viscosity-temperature relation to the low-temperature range, in which the viscosity data were not available.

Raman spectroscopy

Raman spectra were recorded using a Thermo Nicolet Nexus spectrometer with a neodymium-doped yttrium aluminium garnet (Nd:YAG) laser (1064 nm), and the spectral resolution was 4 cm^{-1}. A typical power of 0.1 W was used to record spectra in the range of 100 to 3500 cm^{-1}.

X-ray photoelectron spectroscopy

XPS measurements were performed by an ESCALAB 250Xi x-ray photoelectron spectrometer using Al K_α radiation. The spectra were calibrated by referencing the binding energy of carbon (C 1s, 284.6 eV).

Solution NMR spectroscopy

Solution ^1H NMR spectra of digested samples [in a mixture of DCl (35%)/D_2O (0.1 ml) and dimethyl sulfoxide–d_6 (DMSO-d_6; 0.5 ml)] of desolvated crystalline ZIF-62 samples and the ZIF-62 glasses (about 6 mg) were recorded on a Bruker Avance III 500 MHz spectrometer at 293 K. Chemical shifts were referenced to the residual protio-solvent signals of DMSO-d_6. The spectra were processed with the MestreNova Suite.

Positron annihilation lifetime spectroscopy

PALS measurements were performed using an identical sample analysis methodology to that reported literature. The samples were measured on an EG&G Ortec fast-fast coincidence system using NaCl (~1.5×10^6 becquerel), which was sealed in a thin Mylar envelope. The samples in the form of powders were packed into a vacuum cell located 2 mm on each side of the positron source. The measurements were taken under vacuum (1×10^{-5} torr) at 298 K, and 4.5×10^6 integrated counts per file for each sample were collected. A source correction of 1.48 ns and 3.033% was subtracted from each spectrum. The spectra were deconvoluted using the LT v.9 software. Each spectrum was fitted to four components, with the first two components fixed to 0.125 ns (para-positronium) and approximated to 0.4 ns (free annihilation). The third and fourth components were due to ortho-positronium (o-Ps) annihilation events indicating the presence of two distinct pore sizes within the materials. Table S2 lists the fitted parameters including o-Ps intensity and lifetime for each sample along with the calculated pore diameters and fractional free volume used.

Solid-state NMR spectroscopy

Solid-state NMR experiments were carried out on a 600-MHz Varian NMR system equipped with a 1.6-mm Varian HXY CPMAS probe. Larmor frequencies for ^1H and ^{13}C were 599.51 and 150.75 MHz, respectively, and sample rotation frequency was 40 kHz. For one-dimensional ^1H MAS and ^1H-^{13}C CPMAS measurements, ^1H 90° excitation pulse of 1.25 μs was used. The CPMAS experiment used ramped-amplitude (RAMP) CP block, with duration of 4 ms, and high-power X-inverse X (XiX) heteronuclear decoupling during acquisition; the number of scans was 6000, and repetition delay between scans was 1 s. For two-dimensional ^{13}C-detected spin-diffusion measurements, the number of scans was 5000, number of increments in indirectly detected dimensions was 12, and repetition delay between scans was 0.5 s. The experiments used the Lee-Goldburg scheme during the 100-μs-long CP block and high-power XiX heteronuclear decoupling during acquisition. Frequency axes of ^1H and ^{13}C spectra were referenced to tetramethylsilane. Detailed information for calculating density deficit, entropy and enthalpy of fusion, and the analysis of NMR results and mechanical moduli can be found in the Supplementary Materials.

SUPPLEMENTARY MATERIALS

Supplementary material for this article is available at http://advances.sciencemag.org/cgi/content/full/4/3/eaao6827/DC1

Supplementary Methods

fig. S1. Phase structure evolution with heating temperature.

fig. S2. Comparison of valence states between crystal and glass.

fig. S3. Porosity in MQ ZIF-62 glass.

fig. S4. Porosity in MQ ZIF-62 glass.

fig. S5. Determination of liquid fragility index (*m*).

fig. S6. The appearance change of the MQ ZIF-62 glass with heating temperatures.

fig. S7. XRD patterns of nonstoichiometric ZIF-62.

fig. S8. Characterization of linker ratios.

fig. S9. Influence of linker substitution on T_m and T_g.

fig. S10. Characterization of linker distribution.

fig. S11. Characterization of linker distribution.

fig. S12. Characterization of linker distribution.

fig. S13. Schematic representation of linker substitution.

fig. S14. Poisson's ratio of ZIF-62 crystal and glass.

table S1. Synthesis parameters for ZIF-62.

table S2. PALS data for ZIF-4 glass and ZIF-62 glass.

table S3. Evolution of the thermodynamic parameters and T_g with increasing blm.

table S4. T_g/T_m, T_m, and glass-crystal density deficit $\Delta\rho/\rho_g$ for the materials highlighted in Fig. 4.

References (*37*–*42*)

REFERENCES AND NOTES

1. T. D. Bennett, J.-C. Tan, Y. Yue, E. Baxter, C. Ducati, N. J. Terrill, H. H.-M. Yeung, Z. Zhou, W. Chen, S. Henke, A. K. Cheetham, G. N. Greaves, Hybrid glasses from strong and fragile metal-organic framework liquids. *Nat. Commun.* **6**, 8079 (2015).
2. D. Umeyama, S. Horike, M. Inukai, T. Itakura, S. Kitagawa, Reversible solid-to-liquid phase transition of coordination polymer crystals. *J. Am. Chem. Soc.* **137**, 864–870 (2015).
3. Y. Zhao, S.-Y. Lee, N. Becknell, O. M. Yaghi, C. A. Angell, Nanoporous transparent MOF glasses with accessible internal surface. *J. Am. Chem. Soc.* **138**, 10818–10821 (2016).
4. C. A. Angell, Formation of glasses from liquids and biopolymers. *Science* **267**, 1924–1935 (1995).
5. G. N. Greaves, S. Sen, Inorganic glasses, glass-forming liquids and amorphizing solids. *Adv. Physiol. Educ.* **56**, 1–166 (2007).
6. K. Ito, C. T. Moynihan, C. A. Angell, Thermodynamic determination of fragility in liquids and a fragile-to-strong liquid transition in water. *Nature* **398**, 492–495 (1999).
7. L.-M. Wang, C. A. Angell, R. Richert, Fragility and thermodynamics in nonpolymeric glass-forming liquids. *J. Chem. Phys.* **125**, 074505 (2006).
8. E. D. Zanotto, D. R. Cassar, The microscopic origin of the extreme glass-forming ability of Albite and B_2O_3. *Sci. Rep.* **7**, 43022 (2017).
9. U. Ali, K. J. Bt. A. Karim, N. A. Buang, A review of the properties and applications of poly (methyl methacrylate) (PMMA). *Polymer Rev.* **55**, 678–705 (2015).
10. P. Y. Huang, S. Kurasch, A. Srivastava, V. Skakalova, J. Kotakoski, A. V. Krasheninnikov, R. Hovden, Q. Mao, J. C. Meyer, J. Smet, D. A. Muller, U. Kaiser, Direct imaging of a two-dimensional silica glass on graphene. *Nano Lett.* **12**, 1081–1086 (2012).
11. J. C. Phillips, Topology of covalent non-crystalline solids I: Short-range order in chalcogenide alloys. *J. Non Cryst. Solids* **34**, 153–181 (1979).
12. P. K. Gupta, A. R. Cooper, Topologically disordered networks of rigid polytopes. *J. Non Cryst. Solids* **123**, 14–21 (1990).
13. J. C. Mauro, Topological constraint theory of glass. *Am. Ceram. Soc. Bull.* **90**, 31–37 (2011).
14. G. N. Greaves, F. Meneau, A. Sapelkin, L. M. Colyer, I. Ap Gwynn, S. Wade, G. Sankar, The rheology of collapsing zeolites amorphized by temperature and pressure. *Nat. Mater.* **2**, 622–629 (2003).
15. K. S. Park, Z. Ni, A. P. Côté, J. Y. Choi, R. Huang, F. J. Uribe-Romo, H. K. Chae, M. O'Keeffe, O. M. Yaghi, Exceptional chemical and thermal stability of zeolitic imidazolate frameworks. *Proc. Natl. Acad. Sci. U.S.A.* **103**, 10186–10191 (2006).
16. P. Z. Moghadam, A. Li, S. B. Wiggin, A. Tao, A. P. G. Maloney, P. A. Wood, S. C. Ward, D. Fairen-Jimenez, Development of a Cambridge Structural Database Subset: A collection of metal–organic frameworks for past, present, and future. *Chem. Mater.* **29**, 2618–2625 (2017).
17. T. D. Bennett, Y. Yue, P. Li, A. Qiao, H. Tao, N. G. Greaves, T. Richards, G. I. Lampronti, S. A. T. Redfern, F. Blanc, O. K. Farha, J. T. Hupp, A. K. Cheetham, D. A. Keen, Melt-quenched glasses of metal–organic frameworks. *J. Am. Chem. Soc.* **138**, 3484–3492 (2016).
18. H. Tao, T. D. Bennett, Y. Yue, Melt-quenched hybrid glasses from metal–organic frameworks. *Adv. Mater.* **29**, 1601705 (2017).
19. R. Gaillac, P. Pullumbi, K. A. Beyer, K. W. Chapman, D. A. Keen, T. D. Bennett, F.-X. Coudert, Liquid metal–organic frameworks. *Nat. Mater.* **16**, 1149–1154 (2017).
20. P. W. Anderson, Through the glass lightly. *Science* **267**, 1615–1616 (1995).
21. G. Kumari, K. Jayaramulu, T. K. Maji, C. Narayana, Temperature induced structural transformations and gas adsorption in the zeolitic imidazolate framework ZIF-8: A Raman study. *J. Phys. Chem. A* **117**, 11006–11012 (2013).
22. S. Gadipelli, W. Travis, W. Zhou, Z. Guo, A thermally derived and optimized structure from ZIF-8 with giant enhancement in CO_2 uptake. *Energy Environ. Sci.* **7**, 2232–2238 (2014).
23. A. Schneemann, V. Bon, I. Schwedler, I. Senkovska, S. Kaskel, R. A. Fischer, Flexible metal–organic frameworks. *Chem. Soc. Rev.* **43**, 6062–6096 (2014).
24. A. W. Thornton, K. E. Jelfs, K. Konstas, C. M. Doherty, A. J. Hill, A. K. Cheetham, T. D. Bennett, Porosity in metal–organic framework glasses. *Chem. Commun.* **52**, 3750–3753 (2016).
25. J. C. Mauro, Y. Yue, A. J. Ellison, P. K. Gupta, D. C. Allan, Viscosity of glass-forming liquids. *Proc. Natl. Acad. Sci. U.S.A.* **106**, 19780–19784 (2009).
26. J. Orava, A. L. Greer, Fast and slow crystal growth kinetics in glass-forming melts. *J. Chem. Phys.* **140**, 214504 (2014).
27. M. Gustafsson, X. Zou, Crystal formation and size control of zeolitic imidazolate frameworks with mixed imidazolate linkers. *J. Porous Mat.* **20**, 55–63 (2013).
28. P. Richet, Y. Bottinga, Rheology and configurational entropy of silicate melts. *Rev. Mineral.* **32**, 67–93 (1995).
29. G. P. Johari, A. Hallbrucker, E. Mayer, The glass–liquid transition of hyperquenched water. *Nature* **330**, 552–553 (1987).
30. Y. Yue, C. A. Angell, Clarifying the glass-transition behaviour of water by comparison with hyperquenched inorganic glasses. *Nature* **427**, 717–720 (2004).
31. G. N. Greaves, A. L. Greer, R. S. Lakes, T. Rouxel, Poisson's ratio and modern materials. *Nat. Mater.* **10**, 823–837 (2011).
32. Y.-Z. Yue, Characteristic temperatures of enthalpy relaxation in glass. *J. Non Cryst. Solids* **354**, 1112–1118 (2008).
33. V. M. Fokin, M. L. F. Nascimento, E. D. Zanotto, Correlation between maximum crystal growth rate and glass transition temperature of silicate glasses. *J. Non Cryst. Solids* **351**, 789–794 (2005).
34. W. H. Wang, Correlations between elastic moduli and properties in bulk metallic glasses. *J. Appl. Phys.* **99**, 093506 (2006).
35. W. Tu, X. Li, Z. Chen, Y. D. Liu, M. Labardi, S. Capaccioli, M. Paluch, L.-M. Wang, Glass formability in medium-sized molecular systems/pharmaceuticals. I. Thermodynamics vs. kinetics. *J. Chem. Phys.* **144**, 174502 (2016).
36. J. D. Stevenson, P. G. Wolynes, Thermodynamic–kinetic correlations in supercooled liquids: A critical survey of experimental data and predictions of the random first-order transition theory of glasses. *J. Phys. Chem. B* **109**, 15093–15097 (2005).
37. C. J. Pickard, F. Mauri, All-electron magnetic response with pseudopotentials: NMR chemical shifts. *Phys. Rev. B* **63**, 245101 (2001).
38. J. R. Yates, C. J. Pickard, F. Mauri, Calculation of NMR chemical shifts for extended systems using ultrasoft pseudopotentials. *Phys. Rev. B* **76**, 024401 (2007).
39. R. Banerjee, A. Phan, B. Wang, C. Knobler, H. Furukawa, M. O'Keeffe, O. M. Yaghi, High-throughput synthesis of zeolitic imidazolate frameworks and application to CO_2 capture. *Science* **319**, 939–943 (2008).
40. M. Xiong, N. Li, G. N. Greaves, Y. Z. Yue, X. J. Zhao, Quantum chemical calculations to elucidate the electronic and elastic properties of topologically equivalent metal organic frameworks. https://arxiv.org/abs/1712.07372 (2017).
41. K. V. Tian, B. Yang, Y. Yue, D. T. Bowron, J. Mayers, R. S. Donnan, C. Dobó-Nagy, J. W. Nicholson, D.-C. Fang, A. L. Greer, G. A. Chass, G. N. Greaves, Atomic and vibrational origins of mechanical toughness in bioactive cement during setting. *Nat. Commun.* **6**, 8631 (2015).
42. Y. Y. Wang, H. Nakanishi, Y. C. Jean, T. C. Sandreczki, Positron annihilation in amine-cured epoxy polymers—Pressure dependence. *J. Polym. Sci. B* **28**, 1431–1441 (1990).

Acknowledgments

Funding: A.Q., H.T., G.N.G., J.C.M., and Y.Y. thank the National Natural Science Foundation of China (no. 51772223), the "1000 Talents" Program of China, the "Strategy Scientists" Program of Wuhan University of Technology, and Corning Incorporated for the support. T.D.B. would like to thank the Royal Society for a University Research Fellowship. A.K. and G.M. acknowledge the support of the Slovenian Research Agency. C.M.D. acknowledges the Australian Research Council Discovery Early Career Researcher Award (DE140101359) and the Veski Inspiring Women Fellowship for the support. A.W.T. acknowledges the Julius Career Award from the Commonwealth Scientific and Industrial Research Organization for the support (2014 to 2017). **Author contributions:** Y.Y. conceived the project. H.T., A.Q., T.D.B., and Y.Y. designed the experimental route. G.N.G., Y.Y., A.Q., H.T., and T.D.B. wrote the manuscript. All authors discussed the results and revised the manuscript. A.Q. prepared the

samples and performed the DSC, XRD, Raman, liquid NMR, and XPS measurements and analysis, guided by T.D.B., G.N.G., H.T., and Y.Y. H.T. and A.Q. performed the viscosity study. C.M.D. and A.W.T. conducted the PALS experiments and analyzed the data. A.K. and G.M. performed the solid NMR study. J.C.M. facilitated the mechanical characterizations.
Competing interests: The authors declare that they have no competing interests. **Data and materials availability:** All data needed to evaluate the conclusions in the paper are present in the paper and/or the Supplementary Materials. Additional data related to this paper may be requested from the authors.

Submitted 15 August 2017
Accepted 1 February 2018
Published 9 March 2018
10.1126/sciadv.aao6827

Citation: A. Qiao, T. D. Bennett, H. Tao, A. Krajnc, G. Mali, C. M. Doherty, A. W. Thornton, J. C. Mauro, G. N. Greaves, Y. Yue, A metal-organic framework with ultrahigh glass-forming ability. *Sci. Adv.* **4**, eaao6827 (2018).